AMS Home   Journals Home   Journal Archive   Subscribe   For Authors   Help   Advanced Search   [Search] Go

Full Text View

Convection in Small Basins

William K. Dewar

Department of Oceanography, The Florida State University, Tallahassee, Florida

ABSTRACT

Convection in the world's oceans often occurs in small, semienclosed basins where bottom slopes and nearby continental shelf breaks are commonplace. The evolution of convectively generated heat anomalies in such settings is studied using quasigeostrophic finite-difference and point vortex models. The displayed behaviors divide essentially into two categories: whole fluid column convection, in which bottom-slope effects are felt immediately, and partial fluid column convection, in which the topographic effects can be delayed. In both cases, topography significantly modifies the evolution of convective patches from that occurring over flat bottoms. Vertical walls induce strong self-propagation mechanisms that accelerate alongslope heat transport, while the continental shelf slope is repulsive and rejects lower-layer anticyclones. These anomalies are then "stranded," being too far offshore to interact with the shelf break and having lost their heton partner in the interaction. Weaker deep ocean topographic slopes disrupt heton formation and disperse convective patches by topographic mechanisms. Partial fluid column convection, with stratification under the mixed layer, proceeds through a cascade from small to large length scales. In oceanically relevant regimes, smaller scales are shielded from bottom slopes and can disperse as small hetons. Larger-scale structures are prevented by the topography from forming into hetons and instead evolve as if in a sloping-bottom two-layer system. The small hetons, when encountering shelf breaks, can experience topographic repulsion and stranding. Comparisons with the Mediterranean Sea suggest alternative interpretations for some observations, and several observed Labrador Sea mesoscale convective characteristics can be ascribed to topographic effects.

1. Introduction

Send et al. (1996) have shown that Mediterranean water masses formed in a convective event appeared later in a nearby topographically trapped current. The convection was part of the well-known Mediterranean water mass formation occurring south of Marseilles in the Gulf of Lions. Other well-known and well-studied convection sites include the Labrador Sea and the Greenland Sea (Lilly et al. 1999; Marshall and Schott 1999; Lilly et al. 2001, manuscript submitted to *J. Phys. Oceanogr.*). All three seas are semienclosed and possess complex topography, including bottom slopes and continental shelf breaks. This and the observations of Send et al. (1996) suggest strongly that basin and continental topography can affect the dispersal of convectively formed water masses. This problem is studied here in idealized settings modeled after the observed basins. The results argue topography plays a fundamental role in both the dispersion and retention of newly formed deep

waters. Comparisons with the Mediterranean and Labrador Seas are favorable and alternative interpretations of some of the data are suggested. To the extent that many, and perhaps all, water mass sites neighbor continental boundaries, the interactions discussed here are of general significance to water mass dispersal.

a. Background

Deep convection has been frequently studied in the marginal seas of the North Atlantic. A comprehensive review appears in Marshall and Schott (1999), who discuss observational programs in the Mediterranean, Labrador, and Greenland Seas and modern developments in theoretical, numerical, and laboratory investigations of convection.

1) OBSERVATIONS

Send et al. (1996) build on earlier convection measurements by the MEDOC Group (1970). That study documented the role of the mistral winds in driving the overturning and the extreme vertical velocities characteristic of active convection. The THETIS program (the THETIS Group 1994), from which the Send et al. (1996) analysis comes, extended these observations by documenting the regional distribution of the overturning and the apparent dispersal of the convectively formed waters along the Mediterranean continental slope. The latter suggested a new mechanism for convective dispersal by entrainment into a boundary current, the plausibility of which had been raised by numerical investigation (Hallberg and Rhines 1996). Greenland Sea convection was the subject of an observational program in the late 1980s. Schott et al. (1993) describe various aspects of the preconditioning phase and "deep" (1500 m) Greenland convection in 1988. The Labrador Sea has long been recognized as a site of deep convection because of the presence of Labrador Sea Water throughout the North Atlantic. Talley and McCartney (1982) described its distributions and pathways by exploiting potential vorticity. Gascard and Clarke (1983) and Clarke and Gascard (1983) discuss direct observations of convective events in the Labrador Sea. Pickart (1992) documented Labrador Sea Water distribution along the North Atlantic western boundary. In addition, the Labrador Sea was the site of an intensive field program, the results of which are now emerging (the LabSea Group 1998).

Important characteristics of convective sites appear in Figs. 1–3. The first is a plan view of the Gulf of Lions. Convection is typically centered offshore of the gulf in about 2000 m of fluid, although the bottom changes over the area by about 500 m. The convection site itself is roughly $(100 \text{ km})^2$. Nearer shore, the shelf break appears, characterized by 500-m depth changes occurring over 10 km and there is an intensification of the bottom slope southwest of the convection site. Also shown in this figure are the locations of two mooring sites (labeled H and J) associated with the THETIS program.

Mediterranean convection often reaches the bottom, as shown in Fig. 2. The upper panel is mixed layer depth from a simulation of the Gulf of Lions convection in 1994 (Send et al. 1996). Deep convection lasts about one month with the mixed layer spanning the entire fluid column around 10 February. The lower panel is the mixed layer temperature from this same simulation and shows the period of slow temperature change associated with the deepest mixed layers. As shown in Send et al., cold anomalies were observed 100 km away at the southwestern J mooring site in early March, that is, about one month after the convective event.

Figure 3 is a potential density transect from the Labrador Sea (Marshall and Schott 1999). The structure is dominated by a weakly stratified pool, extending from a few hundred meters to roughly 2000 m, that is a remnant of previous deep mixing. Labrador Sea convection is thus "partial" in that it does not reach through the entire water column. Typical topographic variation in the Labrador Sea also appears in this figure. Away from the coasts, the bottom slopes are comparable to, if a bit weaker than, those in the Mediterranean. Nearer shore are continental slopes of hundreds of meters depth change over a few kilometers in the horizontal. These occur over the entire depth range of the convection (down to 2000 m).

2) THEORY AND LABORATORY STUDIES

Send et al. (1996) rooted their interpretation of the THETIS observations at least partly in Hallberg and Rhines (1996), although that study focused on the generation of topographic currents by convection rather than on entrainment by existing currents. Hallberg and Rhines pointed out the control that continental slopes can have on the distribution of convectively formed waters due to their effects on planetary vorticity. These effects differed for differing depth ranges because of the differing locations of topography–isopycnal intersection. Hallberg and Rhines (2000) discuss gyre circulations in the presence of geophysically relevant topography with an emphasis on potential vorticity budgets.

Maxworthy and Narimousa (1994) developed scaling laws for the characteristics of convective vortices in the laboratory. Helfrich (1994) examined convective plume evolution in a rotating system and Brickman (1995) studied equilibrium convective patch properties. Coates and Ivey (1998) studied finite patch sizes abutting vertical walls in the laboratory. Gawarkewicz and Chapman (1995) examined this problem numerically and recently Boubnov and Rhines (2002, manuscript submitted to *J. Fluid Mech.*) have looked into convection in bowl-shaped basins.

The laboratory results have motivated nonhydrostatic modeling (Jones and Marshall 1993, 1997), which has supported the scaling laws and shown the role of baroclinic vortices (hetons) in the distribution of convectively formed water. The latter has been studied very cleverly using point vortices by Legg and Marshall (1993). Gryanik et al. (2000) generalize the point vortex approach to three dimensions and partial column convection. An attempt at simulating the observed 1992 Labrador Sea convection season using a nonhydrostatic model was reported in Marshall and Schott (1999), where the developing baroclinic instability of the convective patch was noted. Madec et al. (1991) computed convective patch evolution with

application to the Mediterranean.

b. This paper

The objective of the present work is to examine if and how convection will be influenced by oceanically relevant topography. The numerical studies of Hallberg and Rhines (1996) are extended here by a focus on the mesoscale dynamics of a convective patch, rather than the general circulation consequences of convection, and in the use of a finite duration surface buoyancy flux. Types of topography different than the bowl-shaped basin that was their emphasis are also considered. Relative to Legg and Marshall (1993) and Gryanik et al. (2000), nearby topography is included in point vortex calculations and they are complemented with finite-difference quasigeostrophic model investigations. Three-layer models as well as two-layer models are studied and new effects are found. Our interest in the Mediterranean complements Madec et al. (1991) in the inclusion of topography and in the Labrador Sea problem complements Marshall and Schott (1999) by using mesoscale resolution.

We believe that quasigeostrophy (QG) is a useful dynamical tool to investigate this problem, due largely to the success of point vortex models in conceptualizing the nonhydrostatic results in Jones and Marshall (1993). The value of the heton convection model was demonstrated in Legg et al. (1996), who showed that their equilibrium characteristics matched those of primitive equation and laboratory convection experiments. This held in neutral and stratified settings, although quasigeostrophy is more restricted than either because of a fixed deformation radius. In addition, as shown by Hallberg and Rhines (1996) in a primitive equation model, the dynamics of a convective patch are governed on long timescales by potential vorticity, which is the centerpiece of QG theory.

Accordingly, it is argued that topography plays several roles in an evolving convective patch and that these are differentiated roughly by the fraction of the fluid column through which the convection extends. For whole column convection, like the Mediterranean, the heton model of convective dispersal is significantly modified by topography. Even relatively modest bottom slopes under convection can direct heat anomalies along isobaths at rates consistent with the observations of Send et al. (1996). For partial fluid column overturning, the heton spreading model is relevant to the early evolution; however, the presence of more layers implies that more vertical modes are involved, and these can interact. Like-signed vortex pairing in layers is an important dynamic effect and drives vortices toward the lowest baroclinic deformation radius. The vertical expressions of these vortices can be quite strong, thus catalyzing interactions with bottom slopes. The sequence can play a role in gyre preconditioning. Some of the eddy characteristics reported by Lilly and Rhines (2002) in the Labrador Sea have analogs in the present calculations. On the other hand, Lilly and Rhines report a lack of observed surface cyclonic vortices. A clear explanation of that is not offered from these calculations, although topography does yield a partial explanation.

The problem of whole column convection is developed in the next section and studied by point vortex and finite difference QG codes. Extensions to three layers are developed in section 3, along with a discussion of the geophysically interesting parameter regime. Partial column evolution is analyzed and the paper concludes with a discussion section.

2. Whole column convection

Perhaps the simplest dynamics relevant to the Mediterranean setting are two-layer, f-plane quasigeostrophy with bottom topography. The equations governing this system are

$$\left[\frac{\partial}{\partial t} + \frac{1}{f_o} J(p_i, \cdot) \right] q_i = \kappa_i \nabla^6 \frac{p_i}{f_o} + (-1)^i \frac{f_o}{H_i} e,$$

$$i = 1, 2$$

$$q_i = \nabla^2 \frac{p_i}{f_o} + (-1)^i \frac{f_o}{H_i} h_1 + \frac{f_o}{H_2} h_b \delta_{i,2},$$

$$(1)$$

with q_i being potential vorticity in layer i, p_i layer pressure, f_o Coriolis parameter, H_i layer thickness, h_b bottom topography, J the Jacobian operator, e the exchange rate of fluid between the layers, κ_i the hyperviscosity coefficient for layer i, perturbations to the interface are given by $h_1 = (p_1 - p_2)/g_1$, and g_1 is interfacial reduced gravity. The quantity $\delta_{i,2}$ denotes the Kronecker delta function.

Deformation radii associated with convection are usually small because, as shown in laboratory and numerical experiments, vortices develop from weak, convectively generated density differences (Legg et al. 1996). This is modeled in the present setting by $g' = 0.002$ m s^{-2} and $H_1 = H_2 = 1000$ m, which yields a deformation radius, R_d, of 10 km, similar to that observed in the Mediterranean. Two key parameters are the ratios of R_d to the initial patch distance from the boundary, y_o, and the initial patch scale, r_o. Gulf of Lions convection typically occurs several deformation radii away from the

boundary and with patch scales large compared to the deformation radius (see Fig. 1 ⊙). This is reflected here by choosing $R_d/y_o \ll R_d/r_o \ll 1$ (see Fig. 4 ⊙). The latter corresponds to the regime studied by Gawarkewicz and Chapman (1995) and Coates and Ivey (1998), while the former differs in that they studied $R_d/y_o \sim 1$. The present parameters imply the patch evolves in the absence of the boundary and brings in topography as an influence on heton dispersion. Another key factor is buoyancy flux, which controls the amplitude of thermocline anomaly. Dimensional analysis argues the role of this parameter relative to topographic amplitudes; these will be discussed in the following subsections.

a. Side walls

The simplest topographic effect, but perhaps the least relevant, can be demonstrated using a vertical side boundary in a flat-bottomed basin. Point vortices are a convenient method for studying this problem and their use connects the present study to published results. Point vortex implementation is discussed in the appendix; a basin schematic appears in Fig. 4 ⊙.

The evolution of a point vortex system appears in Fig. 5 ⊙. Surface heat loss to the atmosphere of 250 W m^{-2} was applied over a circular region of 50-km radius for 30 days. Other parameters are as discussed previously or as in the appendix. The center of the heat loss disk was 125 km offshore of the northern boundary. Every 6 hours, a vortex representing 6 h of surface heat flux was introduced at a random location in the convective site. Figure 5 ⊙ shows vortex distributions at days 45, 90, 135, and 180. The early evolution is dominated by rim current baroclinic instability and heton formation (Legg and Marshall 1993). The novel boundary effect occurs when the northern hetons approach the wall. At a few deformation radii, they come under the influence of boundary images, which drive the anticyclones (cyclones) east (west). Same layer image interactions grow in strength with decreasing separation, so point vortices a deformation radius from the boundary move faster than a heton pair with comparable separation. Alongslope heat dispersal can thus exceed the east–west dispersal of anomalous water in the open ocean. This appears in Fig. 6 ⊙ showing the rms separation from the convection center of vortices plotted against time. The upper two curves are from the nearshore experiment and represent the dispersions of the cyclonic and anticyclonic members separately. The lower curve, measuring dispersion in an unbounded domain, clearly lags the former results. The apparent dominance of the cyclonic members is due to a statistical fluctuation in this particular experiment. (A very early heton contacted the boundary west of the convection site. Cyclones moved west in an unimpeded spread, while the anticyclones moving east encountered vortices from the convection site and were interrupted in their spread.)

Equations (1) in a flat-bottom basin and with convection modeled as an interfacial transfer, e, have also been solved using finite differences. The reduced gravity of the interface was set to 0.002 m s^{-2}, and the layer thicknesses were each 1000 m, yielding a deformation radius of 10 km. The convection was driven for one month by a spatially and temporally constant heat flux of 250 W m^{-2} over a circular site of radius 75 km. This heat flux generated a net thickness anomaly of about 200 m. The convection was centered 125 km offshore in a basin 2500 km by 1000 km. Grid resolution was 2.5 km. Hyperviscosity with coefficient -1×10^9 m^4 s^{-1} and superslip boundary conditions were used. For flat bottoms, the evolution mirrors the point vortex results. Maps of potential vorticity in the upper and lower layers for a representative experiment appear in Fig. 7 ⊙ (only part of the domain is shown).

These experiments suggest that the organizing effect of a boundary can disperse newly formed water masses by a mechanism different from both heton explosion (Legg and Marshall 1993) and boundary current entrainment (Send et al. 1996). This dispersion is also possibly more efficient than that driven by hetons. Variants on these experiments in the next sections, however, argue the image scenario might be of secondary importance.

b. Finite shelfbreak effects

Reexamining Fig. 1 ⊙, it is clear that the previous model at best crudely captures the Gulf of Lions topography, and at worst misses important effects. In particular, the shelf break is not vertical; rather, it slopes upward at a rate of 500 m over about 10 km. The latter length scale is close to the heton deformation radius, so it is plausible an approaching heton will see the break as a gradient in depth rather than as a wall.

This is investigated using the above two-layer finite-difference QG model. Point vortex or contour dynamics approaches are possible, but cumbersome because of the slope. Model equations are (1), now with nonzero h_b, implying the usual QG restriction that topography appears only in the lower layer. Regarding buoyancy flux, typical convective thermocline anomalies, given model stratification, are $\delta h \sim 200$ m (see appendix). Pressure anomalies can thus be scaled by $\delta p \sim g'\delta h$. Lengths are scaled by the patch size L. After some algebra, q_2 is seen nondimensionally to be

$$ q_2 \simeq \frac{R_d^2}{L^2}\nabla^2 p_2 + (p_1 - p_2) - \frac{sL}{\delta h}y, \qquad (2) $$

where s is the (assumed constant) bottom slope. The role of topography is thus measured by $sL/\delta h$, that is, the net topographic depth change over the patch relative to the forced thermocline anomaly. If this ratio is small, evolution should proceed as if in a flat bottom setting. For Mediterranean shelfbreak parameters, $sL/\delta h > O(1)$, suggesting topography should play a dominant role. Convection proceeds offshore of the break, however, so the influence of the shelf break comes in the evolution of the hetons rather than in the evolution of the convective patch. This reflects the parameter choices involved in

patch placement and size. Bottom topography consisted of a shoaling of 500 m over the northernmost 50 km of the model. Note that this slope is weaker by a factor of 5 than the Gulf of Lions shelf break. The convection patch was oval shaped, but aside from this, model heat fluxes, flux duration, and other model parameters were the same as the flat-bottomed case.

Potential vorticity from days 30 and 365 (i.e., the end of the experiment) appears in Fig. 8 . The earlier plot occurs just after the convection has ended and shows the oblong shape of the convection patch. The very early stages of this run are like the flat-bottom case, as is expected. The patch breaks into hetons due to the baroclinic instability of the patch. Four hetons in this experiment move away from the convection site, with two moving parallel to the northern boundary, one south, and one north toward the boundary. The first three behave as open-ocean hetons for the duration of the experiment, essentially self-propagating and carrying with them recently convected fluid. The northern directed heton, however, yields a novel behavior; its trajectories appear in Fig. 9 . Based on the flat-bottom experiment, this heton is expected to encounter its images and spread east and west along the boundary. Instead, the second-layer anticyclonic heton member separates from its surface partner prior to reaching the boundary. Propagation continues for the upper-layer member, although at less than 0.01 m s^{-1} (see Fig. 9), it is weaker than for the flat-bottom case. The lower-layer member, however, remains nearly stagnant in the water, and its subsequent evolution is dominated by a slow, viscously driven decay.

The cause of this behavior appears in Fig. 10 of two high-spatial-resolution views of the above heton interacting with the shelf break. The particular times shown bracket the interesting period of vortex–shelfbreak interaction. The important events occur in the second layer, where the anticyclonic circulation entrains fluid from the shelf break into the deep ocean. The upper panels in this figure are of potential vorticity anomaly and the lower ones are of total potential vorticity. The shelf break is suppressed in the upper panels, making the view of the advected potential vorticity anomaly clearer. The off-break advection creates strong cyclonic lower-layer vorticity on the eastern side of the anticyclone. This circulation drives the anticyclone back offshore by dipole interaction. The repulsion of the anticyclone is overpowering, but the hetonic upper-layer cyclonic flow is only weakly affected due jointly to being physically farther from the lower cyclone and in a separate layer. As a result, the heton complex is broken apart. The upper-layer anomaly, depending on the details of the interaction, can come under the influence of its image and move westward along the wall. There is an indication of this in the experiment shown here but, in all cases studied, the strength of the image interaction, and subsequent self-propagation, was weaker than the flat-bottom case. This is due mostly to being stranded farther offshore than in the flat-bottom case.

A second interesting result is that any lower-layer anticyclones so affected essentially stagnate because they are stripped from their hetonic partner and repulsed to deep water. Their cyclonic neighbor of shelfbreak origin forms a dipole partner but, for a variety of reasons, this configuration is not robust (e.g., the partners are not equal in strength); see also the discussion in Radko (2001, manuscript submitted to *Rec. Adv. Phys. Oceanogr.*). In the present experiments, after moving a few deformation radii into the interior, the dipolar pair break up and the anticyclone stagnates.

The remaining evolution of the stripped anticyclone is then dominated by viscous decay and occasional close passes of other lower-layer anticyclones whose origin is either the leftover pool of convectively formed water or other similarly orphaned anticyclones. As a result, the nearshore area of the convective site can develop a nearly nonpropagating, deep anticyclonic flow that balances an upward bulging thermocline. The latter aspect is a well-known observational feature of deep convection sites; namely, their preconditioning toward annual deep convective events due to upward bowing isopycnals. This is a naturally occurring event in this experiment and it is interesting to speculate that such mechanics are relevant to real open-ocean deep convection.

c. Slope effects

A separate feature of the Gulf of Lions in Fig. 1 is the bottom slope offshore of the shelf break. This slope is roughly 5–10 times smaller than that of the shelf break. On the other hand, the topographic beta associated with such a slope still is two orders of magnitude stronger than the planetary beta, that is,

$$\frac{f_o}{H_2} h_y \approx \frac{10^{-4} \text{ s}^{-1}}{1000 \text{ m}} \frac{500 \text{ m}}{50 \text{ km}} \approx 10^{-9} \text{ (m s)}^{-1}.$$

This slope is also particularly significant for the Gulf of Lions setting, as the convection both occurs over the slope and reaches the bottom. In terms of the topographic parameter, $sL/\delta h \leq O(1)$, suggesting topography should play a significant role in the evolving patch. The h_b topography in (1) was modified to slopes representing bottom deepenings south of the wall from 100 to 500 m. Basins of 500 km × 643 km were used and the slopes covered the northern half domain, thus placing topography under the convection. The Gulf of Lions deep ocean bathymetry, roughly speaking, amounts to a 500 m change in 50 km. The net depth change is like the strongest model settings, but the slopes are weaker by at least a factor of 5.

Major departures from the flat-bottomed setting occur rapidly in this case (see Fig. 11). The upper (lower) panels are upper- (lower-) layer potential vorticity. For day 30, just after the convection has finished, the patch displays a considerable large-scale departure from the forcing symmetry. In comparison, the flat-bottom experiments required about 90 days to generate asymmetries, and those, being due to baroclinic instability, were on the scale of the deformation radius. These differences are early earmarks that different mechanics control patch evolution here.

An important distinction between flat-bottom and sloped cases is that heton generation is largely disabled in the latter. In

fact, the patch early on starts to spread in the pseudo-westward direction (i.e., with shallow waters to the right of the motion), and this distortion becomes the dominant tendency of the evolving patch. A reason contributing to heton suppression is that lower-layer potential vorticity is controlled by topographic slope, as suggested by the topographic parameter. Thus, local potential vorticity anomalies opposite in sign to those in the upper layer are not present. It is the joining of two such opposite signed anomalies in different layers that leads to heton formation, so the topography undercuts their basis at the outset.

Since topography controls evolution, convective dispersal normal to depth contours is weakened considerably. This shows at day 365 in Fig. 11 ⊙═ in that virtually no convectively tainted water has contacted the northern boundary. In contrast, reasonable signatures of convection appear on the western boundary, having arrived there by topographic steering. The fastest signals are, not surprisingly, barotropic topographic waves, which conduct a pressure signature westward. Baroclinic spreading is considerably slower, but still comparable to those speeds noted for the flat-bottom heton case. For example, comparing the potential vorticity anomaly locations between days 90 and 120 shows westward displacements of 50 km have been achieved. More quantitative measures of heat anomaly movement appear in Fig. 12 ⊙═, where time–longitude plots from various latitudes are given. The latitudes are labeled in each panel, upper-layer potential vorticity anomaly is contoured and the same contour interval $[1 \times 10^{-6} \ (\text{m s})^{-1}]$ and maximum and minimum limits are used for all plots. The solid line in each plot indicates a speed of 2 km day^{-1}; comparable anomaly propagations are common in the upper two panels. The more northern latitudes show little to no westward propagation and weaker signals. This is due to the evolution of the patch, which for the most part is prevented from moving northward across the topography.

It is also worth investigating the extent to which baroclinic pressure propagation can depart from material propagation. This is interesting because the signal reported in Send et al. (1996) is of a cold anomaly, and this may reflect upwelling rather than the arrival of convectively formed fluid. These experiments show that the interface deflections are strongly trapped to the potential vorticity anomalies. This appears in Fig. 13 ⊙═ where plan views of upper-layer potential vorticity are in the upper panels and transects from the latitude $Y = 400$ km of potential vorticity and interface deflection h appear in the lower panels. Potential vorticity has been multiplied by 10^7 in the lower panels. Note, h follows potential vorticity in this system. This is robust, occurring at essentially all latitudes and for all parametric variations. Thermal anomalies observed at any location in this system represent the arrival of convectively formed water rather than a wave feature not necessarily composed of recently formed water. The reasons for the weak baroclinic wave dynamics are the small deformation radius of these experiments and that the bottom slope affects the lower layer only.

3. Partial column convection

Convection in the previous section immediately experienced the bottom. While this seems characteristic of the Gulf of Lions, Labrador Sea convection is shielded from the bottom by relatively strong stratification. This section addresses the extent to which such stratification mutes the effects of bottom slopes.

This problem is studied using a three-layer f-plane QG model, the equations of which are

$$\left[\frac{\partial}{\partial t} + \frac{1}{f_o} J(p_1, \cdot) \right] q_1 = \kappa \nabla^6 \frac{p_1}{f_o} - \frac{f_o}{H_1} e; \qquad q_1 = \nabla^2 \frac{p_1}{f_o} - \frac{f_o}{g_1 H_1} (p_1 - p_2)$$

$$\left[\frac{\partial}{\partial t} + \frac{1}{f_o} J(p_2, \cdot) \right] q_2 = \kappa \nabla^6 \frac{p_2}{f_o} + \frac{f_o}{H_2} e; \qquad q_2 = \nabla^2 \frac{p_2}{f_o} + \frac{f_o}{g_1 H_2} (p_1 - p_2) - \frac{f_o}{g_2 H_2} (p_2 - p_3)$$

$$\left[\frac{\partial}{\partial t} + \frac{1}{f_o} J(p_3, \cdot) \right] q_3 = \kappa \nabla^6 \frac{p_3}{f_o}; \qquad q_3 = \nabla^2 \frac{p_3}{f_o} + \frac{f_o}{g_2 H_3} (p_2 - p_3) + \frac{f_o}{H_3} h_b, \qquad (3)$$

(Click the equation graphic to enlarge/reduce size)

where convection is modeled as an interfacial transfer, e, occurring between the upper two layers only and notation is standard. Parameter choices are governed by the setting in Fig. 3 ⊙═. Note that the remnant Labrador Sea mixed layer fills roughly the upper two-thirds of the water column and that the net potential density change under the deep mixed layer is 5–10 times that seen in the upper layers. Equal layer thicknesses, $H_i = 1000$ m for $i = 1, 3$, are thus chosen and the range from $g_2 = 5g_1$ to $g_2 = 10g_1$ has been studied. (It is almost unavoidable for partial column convection that the reduced gravities under the convection will be large compared to convected layers.)

For $g_1 = 0.002$ m s^{-2} and $g_2 = 0.02$ m s^{-2}, as typically used here, the first and second deformation radii are ~ 37 and ~ 10 km, respectively. In contrast, the first deformation radii observed for the convective sites in the Labrador Sea are roughly 7 km (Lilly and Rhines 2002). The second deformation radius, although not mentioned, must be smaller than this.

A topographic parameter similar to that of the two-layer model emerges in this case. The range of bottom slopes found in the Labrador Sea suggest that it ranges from $sL/\delta h \sim 1$ to $sL/\delta h \gg 1$, while the ratio of the first deformation radius to the

patch scale is small. To study these parameter regimes, given the model deformation radius, the horizontal scales of the convective patch and the topographic slopes are increased so that they obtain comparable lengths relative to the first deformation radius. For example, convective patches of 400-km diameter are used, which is roughly a factor of 10 larger than the first model deformation radius. In comparison, the Labrador Sea convective site is estimated to have been O(100 km) in diameter, which is also about 10 times the observed first deformation radius (Marshall and Schott 1999). Bottom slopes of a few hundred meters over distances like the first deformation radius (typical of the shelf break), or several deformation radii (typical of Labrador Sea bottom slopes) are used. All runs used 2.5-km grid spacing, thus resolving both deformation radii.

a. Flat-bottomed results

Figure 14 shows the relatively early evolution of a convectively generated patch in a flat-bottomed three-layer model, the purpose of which is to provide a benchmark and to illustrate the behaviors expected in a flat-bottom multilayer system. Potential vorticity values characteristic of the convection are shown by solid contours; values close to background values are shown by dashed contours. The buoyancy flux driving convection was maintained at 250 W m^{-2} for 30 days, as in the two-layer experiments.

The early history of the patch is classical, with baroclinic instabilities on the patch rim (see day 90). The fastest growing modes are on the second deformation radius rather than the first. These rim vortices pair vertically into hetons but, as is evident in the later views, a competing effect that dominates their dispersive behavior is like-signed vortex merger. This effect in stratified convective settings was explicitly noticed by Send and Käse (1998); Madec et al. (1991) also show similar results. Gryanik et al. (2000) label such behavior as "confinement" and discuss its relation to initial vortex separation and deformation radius. Comparable evolution occurs in the second layer, while the deepest layer, without potential vorticity anomalies, responds passively.

Dispersal from the convective site is slowed because of merger, and the scales of the irregular vorticity anomaly patches grow. The complete lack of any second-mode heton dispersal is an artifact of the symmetric initial condition. In other experiments (not shown here) with less symmetric convective patches, some second-mode hetons formed on the far edges of the convection and escaped. In all cases, however, the number of second-mode vortices emitted by the patch was a small fraction of the growing undulations initially on the rim current. Suppression of second-mode heton dispersion apparently is a strong tendency for partial column convection.

Later stages of the patch evolution appear in Fig. 15. Clearly, like-signed vortex merging continues until the potential vorticity patches grow to the first deformation radius. At that point, heton pairing takes over and the patch disperses. Gryanik et al. (2000) refer to this behavior as the "splitting" regime. Classical heton explosion appears at days 395 and 425, times at which the meridionally spreading hetons have contacted the domain boundary. After the heton departures, the remaining potential vorticity anomalies begin a like-signed vortex merger sequence again. This is a weaker process because the strength of the remaining potential vorticity anomaly has been considerably reduced.

b. Deep-water slope effects

Having established a flat-bottom evolution for comparison, topographic effects are studied by modifying the experimental setup. The impact of deep slopes under the partial column convection is considered first.

From Fig. 3, bathymetric changes of a few hundred meters over 100 km typify the deep Labrador Sea, while closer to the basin edges, bottom changes of 500 m are found over lateral distances of 10 km. According to Marshall and Schott (1999), the estimated location of Labrador convection was relatively close to the basin edge and thus in a strongly bottom-sloped area. Figure 16 shows the results of an experiment using a constant slope corresponding to a 500-m depth change over 1000 km (about 30 deformation radii). Depending on the location of the convection, this is comparable to or considerably weaker than (by a factor of 30) the relevant slopes in the Labrador Sea. Solid contours in all panels mark potential vorticity of convective origin; dashed lines are of background values.

The early (i.e., 30–90 day) evolution is essentially unchanged from the flat-bottomed case. This is not surprising as the potential vorticity anomalies are introduced into the upper two layers only, and this phase of the evolution reflects Rossby adjustment to the potential vorticity forcing. At day 90, baroclinic instability is evident, and anomalies occur on the second deformation radius as in the flat-bottomed run. Evidence of bottom slope effects appear shortly thereafter. For example, small differences in the day-150 states appear between these two runs, and by day 250, the differences are quite evident. In the present case, with a sloping bottom, one notes the appearance of a small number of small-scale hetons (roughly four) that are separating from the main patch core. Further, the core evolution itself is not as organized as it is in the flat-bottomed case. In the latter case, the bulk of the convectively generated fluid was still closely associated with the initial convective site and local extrema, originally occurring on the small scale, are actively engaged in like-signed vortex merging. Similar mechanics are, of course, present in the experiment in Fig. 16 but are obviously competing with other influences. The anomalies at day 250 in the bottom-slope experiment are smaller and tend to be more zonally elongated than for the flat-bottom experiment.

The differences between the evolution continue at later times. Figure 17 contains plots of upper- and midlayer potential vorticity for days 395 and 425, corresponding to two of the later dates from the flat-bottomed run. The differences in the evolutions of these two systems are by this time quite apparent. Most importantly, for the bottom-slope run, there are

essentially no first-deformation-radius hetons, while in the flat-bottom case, the bulk of the convective fluid has dispersed in them. In fact, there are few indications of active heton pairings in the bottom-slope run. This is evidenced by comparing the upper- and lower-layer potential vorticity anomaly locations, both in the individual snapshots and between the two snapshots. Within snapshots, the upper- and midlayer centers often do not align to form heton pairs. Of those areas that are possible heton pairs, comparing the plots between times shows that for the most part, they do not exhibit pronounced hetonlike propagation tendencies. Often, their displayed evolution is characterized more by one of the partner anomalies shearing the other without any organized propagation. An exception is indicated by the arrows in Fig. 17 **O**▬, which shows an upper- and midlayer pairing that do move in organized hetonlike fashion. However, the lateral scale of this couple is considerably smaller than that observed for the heton couples in the flat-bottom case, suggesting a second-mode structure. Small-scale anomalies are also seen on the northern and southern domain boundaries.

Hetons are a relatively efficient means of dispersing convectively generated waters, but the above experiments suggest heton formation is disabled by bottom slopes. Mass dispersal is thus expected to be less efficient for the latter experiment. This appears in Fig. 18 **O**▬, where mass anomalies within the initial convection site are plotted against time. Data from the second year of the experiments are shown because that is when the flat-bottom run undergoes a heton explosion. The point of this plot is that the sloping-bottom case is considerably more sluggish in dispersing convected waters than is the flat-bottom case. As much as 4 times more mass anomaly remains within the initial convection site in the sloping-bottom experiment than the flat-bottom case.

c. A conceptual model of partial column convection

Analysis of the above behavior is possible using the characteristics of a partially convecting layer. Writing potential vorticity using normal modes (Pedlosky 1979) yields

$$\nabla^2 p_\mu - R_\mu^{-2} p_\mu = f_o q_\mu + \tau_\mu h_b \quad (4)$$

where μ denotes mode (μ is one of the set "b," "$+$," or "$-$"), p_μ and q_μ the normal mode in pressure and its projection onto potential vorticity, respectively, and τ_μ the topographic projection onto mode μ. The quantity R_μ is the deformation radius associated with mode μ. The modes are related to the layer variables for the three-layer problem according to

$$p_b = H_1 p_1 + H_2 p_2 + H_3 p_3;$$

$$q_b = H_1 q_1 + H_2 q_2 + H_3 q_3: \qquad \text{(barotropic mode)}$$

$$p_\pm = p_1 - p_2 + \alpha_\pm(p_2 - p_3);$$

$$q_\pm = q_1 - q_2 + \alpha_\pm(q_2 - q_3): \quad \text{(baroclinic modes),}$$

where notation is standard and

$$\alpha_\pm = 0.5\langle\lambda_1 + 1 - \gamma(1 + \lambda_3)$$

$$\pm \sqrt{\{[\lambda_1 + 1 - \gamma(1 + \lambda_3)]^2 + 4\gamma\}}\rangle \quad (5)$$

with $\lambda_1 = H_1/H_2$, $\lambda_3 = H_3/H_2$, and $\gamma = g_1/g_2$. The deformation radii are related to the eigenvalues and other model parameters via

$$R_\pm^{-2} = f_o^2\left[\frac{1}{g_1}\left(\frac{1}{H_1} + \frac{1}{H_2}\right) - \frac{\alpha_\pm}{g_1 H_2}\right] \qquad (6)$$

and $R_b^{-2} = 0$. The quantities τ_μ in (4) are given by

$$\tau_{[b,\pm]} = \left[-f_o^2, \; \alpha_\pm \frac{f_o^2}{H_3}\right].$$

It is observed for partial column convection that the λ_i thickness parameters are all $O(1)$, but that the stratification parameter $\gamma \ll 1$. In fact, the latter parametric restriction can be taken to define partial column convection. It is thus appropriate to expand (5) in γ.

With $\lambda_1 = \lambda_3 = 1$ (not unlike the Labrador Sea), (5) becomes

$$(\alpha_+, \alpha_-) \simeq (2 - \gamma, -\gamma) + O(\gamma^2) \quad (7)$$

and the two deformation radii are given by

$$(R_{d+}^{-2}, R_{d-}^{-2}) \simeq \frac{f^2}{g_1 H_2}(\gamma, 2 + \gamma) + O(\gamma^2), \quad (8)$$

where R_{d+} denotes the first deformation radius. Scaling potential vorticity and pressure by convective height anomaly δh

$$q_i \approx \frac{f}{H_1}\delta h \quad (9)$$

$$p_i \approx g'\delta h \quad (10)$$

and length by L, the nondimensional mode equations (4) become

$$\nabla^2 p_+ - \frac{f^2 L^2 \gamma}{g_1 H_1}p_+$$

$$= \frac{f^2 L^2}{g_1 H_1}\left[q_1 + q_2 - \gamma q_2 + (2 - \gamma)\frac{sL}{\delta h}\delta y\right]$$

$$\nabla^2 p_- - \frac{f^2 L^2 (2 + \gamma)}{g_1 H_1}p_-$$

$$= \frac{f^2 L^2}{g_1 H_1}\left(q_1 - q_2 - \gamma q_2 - \frac{sL}{\delta h}\delta y\right)$$

$$\nabla^2 p_b = \frac{f^2 L^2}{g_1 H_1}\left(q_1 + q_2 - \frac{sL}{\delta h}\delta y\right), \quad (11)$$

where s represents the bottom slope (taken as a constant) and δy is the Lagrangian displacement of a third-layer fluid parcel from its initial location. The dimensional combination

$$\frac{f_o}{H_3}s\delta y$$

measures the deviation of the potential vorticity in the third layer from its background value. Bottom topography appears in (11) again as the ratio of the net change in bottom topography over the characteristic lateral scale L to the characteristic convectively generated height anomaly. For the Labrador Sea setting, this parameter will be $O(1)$ for lateral length scales L of the first deformation radius.

Consider now the application of these equations to a localized hetonlike potential vorticity anomaly in the upper two layers characterized by a separation on the second deformation radius; that is, $L^2 = O(g_1 H_1/f^2)$. If (11) are then expanded in γ and the definitions of the modes are recalled, there results at leading order

The flat-bottomed, $s = 0$, form of these equations shows p_+ is like the barotropic mode in the two-layer problem and p_- plays the baroclinic mode. Manipulating the equations also demonstrates that $p_3 = O(\gamma)$ in this limit. These results are reassuring because for a large second interface reduced gravity, the upper layers are expected intuitively to decouple from the lower layer. These flat-bottom results generalize to a variable bottom because of the weak lower-layer pressure gradient. First, with L on the second deformation radius, the parameter $sL/\delta h$ is $O((\gamma)^{1/2})$. Further, the Lagrangian displacement δy scales as $O(\gamma)$ because of the weak third-layer pressure. Thus strong stratification under weak stratification makes small second deformation anomalies behave as if in a flat-bottom two-layer model.

If, on the other hand, the characteristic scale L in (11) is chosen to be the first deformation radius, no such simplification is possible. The mode equations become

$$\nabla^2 p_b = \frac{1}{\gamma}\left(q_1 + q_2 - \frac{sL}{\delta h}\delta y\right);$$

$$p_b = p_1 + p_2 + p_3$$

$$\nabla^2 p_+ - p_+ = \frac{1}{\gamma}\left(q_1 + q_2 + 2\frac{sL}{\delta h}\delta y\right);$$

$$p_+ = p_1 + p_2 - 2p_3$$

$$\nabla^2 p_- - \frac{2}{\gamma}p_- = \frac{1}{\gamma}(q_1 - q_2) - \frac{sL}{\delta h}\delta y;$$

$$p_- = p_1 - p_2 \tag{13}$$

and their structure is more complicated than (12). First, the parameter $sL/\delta h$ is now $O(1)$. Also, p_b and p_+ scale as $O(\gamma^{-1})$, implying dimensionally that they are $O(g_2\delta h)$, but that $p_- = O(1)$ still. Thus, the leading-order response is dominantly in the first baroclinic mode and the barotropic mode, and both of these modes experience the bottom at leading order. Larger-scale potential vorticity anomalies are thus strongly exposed to the dispersive character of the bottom topography and not able to sustain the hetonlike character that smaller-scale disturbances can.

A different way of understanding these results comes from computing the projection of the modes on third-layer pressure. Some algebra shows

$$p_3 = \frac{p_b}{3} - \frac{p_+}{3} + \frac{\gamma p_-}{6} - \frac{\gamma p_+}{6}.$$

A leading-order second-mode structure has little presence in the deep layer and generates a barotropic and first baroclinic response that cancel. A leading-order, first-mode structure, however, projects strongly into the third layer and feels the bottom.

These results can be used to explain the numerical experiments in the previous section. The early evolution of the convective patch proceeds as if it were reduced gravity because the patch is large compared to the first deformation radius, and the second interface deforms as needed to shut off lower-layer pressure gradients. The fastest-growing instabilities are on the second deformation radius and develop with weak lower-layer expressions. As a result, this phase proceeds almost identically for the flat- and variable-bottom cases. Some differences do appear and, since the details of the flow differ, even in this very symmetrical case, some heton structures can be ejected by the developing patch. These are necessarily on the second deformation radius and therefore can continue propagating as a small-scale heton. The remaining patch potential vorticity anomalies evolve according to like-signed vortex merger. This explains much of the evolution in the middle panels of Figs. 16 and 17. The upscale cascade in size, however, implies an increasing contact with the dispersive bottom slope, and thus the ever growing influence of the bottom. The evolution in this case becomes more like the sloping-bottom two-layer case, with suppression of heton formation and tendencies for the patch to spread along isobaths.

d. Side wall and shelfbreak effects

The heton dispersal mechanism plays a role in partial column convection, although at smaller scales than the first deformation radius. This then provides a setting in which the flat-bottom two-layer experiments may be applied. In particular, small hetons can encounter side walls and pair up with their images, although this picture will be modified somewhat by the continental shelf break.

In experiments with continental slope–like bottoms confined to the third layer, such slopes did not prevent the small hetons from reaching the boundary (not shown here). It is thus expected that the mechanism of lower-layer anticyclonic heton member rejection, seen in the two-layer experiments, will dominate as the second-layer member of a small heton nears the break.

This result is augmented with one additional experiment designed to comment on the effect of steep side slopes on the cyclonic upper-layer member. This member should be influenced by continental shelf breaks as suggested by the topography in Fig. 3 ⊙. There it is seen that steep shelf breaks characterize the basin sides throughout the water column, and therefore are potential effects for all density ranges. The cyclonic member, as it is driven into an interaction with the lateral boundaries, will be separated from its anticyclonic partner offshore of the location where it will experience the shelf break, but may generally drift into such an interaction.

This case can be crudely examined in the current two-layer quasigeostrophic model by generating a heton pair of the opposite bias, that is, a pair with the cyclone on the bottom and anticyclone on the top. This pair is then permitted to propagate into an interaction with the side boundary, where a shelf break consisting of a 250 m shoaling over the northern 25 km is introduced.

Figure 19 ⊙ shows lower-layer potential vorticity from days 60, 90, 120, and 150 of such an experiment. The interesting result is that the shelfbreak-induced effect on the cyclone is seen to be attractive, rather than repulsive. This results in the cyclone moving rapidly westward along the northern boundary. The later stages of the evolution show the along-shelfbreak dispersal is easily as efficient as open-ocean heton dispersal. Figure 19 ⊙ also displays more than one cyclonic dispersal mechanism. For example, the western cyclone interacting with the shelf break propagates strongly westward as an identifiable coherent structure. On the other hand, the northeastern cyclone interacting with the shelf break is entrained much more strongly onto the break, propagates rapidly westward but disperses because of the topography. While the shelfbreak effect on a cyclone is attractive, subsequent evolution of the cyclone can be varied.

The principal mechanism responsible for cyclonic attraction is the advection onto and off of the break of background waters. This is like the mechanics leading to anticyclonic rejection by a shelf break, and appears in Fig. 20 ⊙. The upper panels are of full lower-layer potential vorticity and the lower panels are of potential vorticity anomaly relative to the topographic effect. Days 90 and 100, bracketing the interesting period of cyclone–shelfbreak interaction in Fig. 19 ⊙, appear. The cyclone advects deep waters onto the topography on its right-hand side. These are anomalously low in potential vorticity relative to the background and therefore spin up an anticyclonic dipole partner that strongly drives the cyclone onto the topography. Cyclones can also advect shelfbreak waters offshore, where they induce a cyclonic circulation. This occurs as input to the northwestward propagating heton in Fig. 20 ⊙. The sense of both induced anomalies is to push the cyclone onto the topography, where it can experience interactions that move it efficiently along the topography.

4. Discussion

The evolution of a convective patch influenced by topography has been examined. The principle effects under consideration are bottom slopes, steep continental shelf breaks, and vertical side walls. The observationally motivated cases of full and partial column convection are considered. Convection generally occurs in relatively small and semienclosed basins, and therefore this study is likely of general importance to water mass dispersal in the real ocean.

Bottom topography appears to be a dominating effect in both full and partial column convection. Full column advection is more strongly affected by bottom topographies, with the most significant impact occurring when the convection occurs over a slope. The settings considered here are modeled after the Gulf of Lions convection site, but the studied bottom slopes are rather modest compared to the real setting. Even for these slopes, heton generation is largely suppressed because the bottom slope dominates convective potential vorticity generation in the lower layer, so upper-layer cyclones are unable to pair with lower-layer anticyclones. Rather, the bottom slope, which is largely dispersive in character, generates psuedowestward baroclinic propagation of the potential vorticity anomalies. Other features of the Mediterranean bottom topography include strong shelf breaks, characterized by depth changes of as much as 500 m over 10 km. Interesting characteristics of heton–shelfbreak interaction include the repulsion of lower-layer anticyclones caused by the hetonic advection of background potential vorticity.

Gawarkewicz and Chapman (1995) numerically and Coates and Ivey (1998) in the laboratory considered the closely related problem of convection on shallow shelves. The convective patches in their settings abutted a vertical wall. Gawarkewicz and Chapman also computed the effects of slopes ranging from 0.001 to 0.005 (like the present experiments) in addition to the flat-bottomed setting. The biggest distinction between these experiments and those discussed in the present paper involves the disruption of the patch geometry by the wall; other differences involved the duration of the experiments (limited to 30 days in Gawarkewicz and Chapman), and five turnover periods in Coates and Ivey (1998). Gawarkewicz and Chapman considered very shallow geometries relative to either the Mediterranean or Labrador Sea setting; their vertical wall was typically 50 m deep, and the deepest fluid extent was a few hundred meters. Coates and Ivey (1998) worked with aspect ratios of order unity. Nonetheless, for these settings and for the timescales involved, both studies emphasized the role of baroclinic instability on the developing rim current, as occurs here. Gawarkewicz and Chapman (1998) found relatively strong cross-bathymetric transport in the deep waters, due most likely to the role of bottom drag in their relatively shallow fluid. Their flat-bottom study suggested the early stages of upper- and lower-layer segregation caused by wall interactions, although the integrations were apparently halted prior to the development of mesoscale wallbound vortices. Comparisons between the laboratory and numerical studies were generally successful. For the times considered, those results correspond to the present results as well.

It is interesting to discuss the observations of Send et al. (1996) in light of these calculations. They documented convection in the Gulf of Lions that reached throughout the water column. A few weeks later, they observed anomalously cold temperatures at a mooring site located west and south of the convection site. Based on the present calculations, these observations can be explained as convection patches spreading pseudowestward along the topography. Model calculations, while highly idealized, show baroclinic propagation rates like those observed. They also support that the cold water seen at the mooring was indeed convective water. This explanation differs somewhat from Send et al. (1996), who suggested convective waters were advected from the region by a boundary current. The present calculations cannot comment on such a scenario because of a lack of a boundary current, so the topographic explanation is offered as an alternative that future observational missions may wish to consider. A second application of these results is that the anticyclonic rejection mechanism can contribute to the preconditioning of the area toward future deep convection events.

The case of partial column advection is motivated by the Labrador Sea and is argued to be more affected by hetonic dispersal, although bottom topography strongly modifies the scenario. Most importantly, such settings are necessarily characterized by a stratified deep layer under a weakly stratified upper ocean. In these circumstances, the second vertical mode, with lateral scales on the second deformation radius, has weak deep-layer expressions while the first mode, with larger lateral scales, has leading-order flows reaching the bottom. The Labrador Sea convective sites are large compared to the first deformation radius, while bottom slopes with depth changes of a few hundred meters can occur over scales from the deformation radius on up. The numerical regimes studied here were like this, although in all cases the bottom slopes were no larger than, and often considerably weaker than, those observed.

The early evolution of the system is dominated by second-mode heton formation. These evolve as hetons due to their weak lower-layer presence and provide a convective dispersal mechanism. On the other hand, within each layer, vortex merger provides a mechanism counteracting dispersion. This effect can be far reaching, operating over lateral scales of the first deformation radius, but as a result of the formation process some second-mode hetons can escape the convective patch. The remaining core begins an upscale cascade in size toward the first deformation radius. Along with this comes an increasing presence in the lowest layer enabling, if a bottom slope is present, bottom dispersion as in the sloping-bottom two-layer case. Nearby lateral boundaries can interact with the second-mode hetons, producing sequences like those for the two-layer cases.

Given the role of multiple deformation radii in the above scenario, it is appropriate to consider the distinctions emphasized by Legg et al. (1996) between QG convective settings and primitive equation/Boussinesq equation convective behavior. The latter systems permit the deformation radii to vary in time during the convection itself, while QG always holds deformation radii at fixed values. The outcome of Legg et al. was that equilibrium properties in QG systems were analogous to those expected in primitive equation settings in spite of the system differences because QG captured the advective mechanics of heton explosions. Details of the time-dependent behavior were not considered, but it is likely QG describes them in the present case for the reason that the interesting behavior occurs after the convection has ceased, at a point where Legg et al. (1996) emphasize the deformation radius becomes fixed in time. Also, the competition between like-signed vortex merger and heton-driven spreading appeared in the primitive equation computations of Send and Käse (1998). The most significant omission in QG dynamics relative to convection and basin boundary interactions is that topographic slopes with intersecting isopycnals are not included. This is an area requiring further study.

There appear to be analogies between these calculations and the recent observations of convective eddies in the Labrador Sea reported by Lilly and Rhines (2002). In particular, they report finding an abundance of vortices of convective origin. Characteristics of these vortices were that they were relatively small compared to the first deformation radius (Lilly and Rhines referred to them as "submesoscale"), frequently appeared to be interacting with neighboring vortices, were often of "composite" structure (i.e., composed of convective waters from more than one year), and were dominantly anticyclonic. In fact, Lilly and Rhines find almost no evidence for cyclonic vortices. Several of these properties can be explained by appealing to the topographic mechanisms discussed here. In particular, the relatively small scales can be ascribed to suppression of first-deformation-scale hetons by topographic dispersion. The nature of the stratification, however, permits second-mode-like hetons to survive, provided they escape the pull of like-signed vortex merger within the patch. The latter point, that the vorticity patches are interacting, is also consistent with the like-signed vortex merger of these experiments. This is a consequence of the partial column convection and the stratification, which allows the vortices to interact over relatively great separations. It has been noted that the dispersal of the convectively formed waters is sluggish if a bottom slope is present, due largely to the suppression of the first-baroclinic-mode heton formation. Thus "old" convective waters remain in the convective site and are available for subsequent convective events. This will naturally yield composite vortices. Also, the current meter analysis in Lilly and Rhines (2002) and Lilly et al. (2001, manuscript submitted to *J. Phys. Oceanogr.*) argued that the deep expression of their convectively formed eddies was weak, leading them to classify these as "surface intensified." Again, this is in agreement with the present results, which argue such structure to be a nature consequence of partial column stratification.

The most curious observation reported by Lilly and Rhines, however, is that they find no cyclones. No complete explanation for that observation emerges from the present calculations. A partial explanation based on topographic effects can be offered, however. This comes from the results that anticyclones interacting with shelf breaks are repulsed while cyclones are attracted. In the Labrador Sea setting, this implies that the surface layer cyclonic vortices will be rapidly evacuated or dispersed from the region by topographic attraction, dispersion, image vortex pairing, and/or along-shelfbreak migration. The anticyclonic vortices, however, will be stranded in the deep ocean, with the only dynamics left being like-signed merger. This scenario is at least qualitatively in agreement with the Lilly and Rhines observations. What it fails to clearly explain is the almost complete absence of cyclones in their data, for the reasons that cyclones still result from the convective patch breakup and migrate the anomalies to the boundary. One would expect some evidence of their existence, if

perhaps less than for the anticyclones. The observation of Lilly and Rhines of an overwhelming dominance of anticyclonic vortices still remains largely unexplained.

A common theme emerging from this work is that topographic interactions are potentially a leading-order effect in the dispersal of convectively formed waters. Although the details differ, this supports the suggestion made in Send et al. (1996) and advanced by Hallberg and Rhines (1996) from numerical work. The contribution here is in the discussion of the effects of the topography on the mesoscale dispersal mechanisms and, in this vein, topography is offered as a controlling influence.

Acknowledgments

REFERENCES

Brickman D., 1995: Heat flux partitioning in open-ocean deep convection. *J. Phys. Oceanogr.*, **25**, 2609–2623. Find this article online

Clarke R., and J.-C. Gascard, 1983: The formation of Labrador Sea water. Part I: Large-scale processes. *J. Phys. Oceanogr.*, **13**, 1764–1778. Find this article online

Coates M., and G. Ivey, 1998: On continental shelf convection: The influence of an ideal coast. *J. Geophys. Res.*, **103**, 15643–15656. Find this article online

Gascard J.-C., and R. Clarke, 1983: The formation of Labrador Sea water. Part II: Mesoscale and smaller-scale processes. *J. Phys. Oceanogr.*, **13**, 1468–1483. Find this article online

Gawarkiewicz G., and D. Chapman, 1995: A numerical study of dense water formation and transport on a shallow, sloping continental shelf. *J. Geophys. Res.*, **100**, 4489–4507. Find this article online

Gryanik V., T. Doronina, D. Olbers, and T. Warncke, 2000: The theory of three-dimensional hetons and vortex-dominated spreading in localized turbulent convection in a fast rotating stratified fluid. *J. Fluid Mech*, **423**, 71–125. Find this article online

Hallberg R., and P. Rhines, 1996: Buoyancy-driven circulation in an ocean basin with isopycnals intersecting the sloping bottom. *J. Phys. Oceanogr.*, **26**, 913–940. Find this article online

Hallberg R., 2000: Boundary sources of potential vorticity in geophysical circulations. *Developments in Geophysical Turbulence,* R. Kerr and Y. Kimura, Eds., Kluwer, 51–65.

Helfrich K., 1994: Thermals with background rotation and stratification. *J. Fluid Mech.*, **259**, 265–280. Find this article online

Jones H., and J. Marshall, 1993: Convection with rotation in a neutral ocean: A study of open ocean deep convection. *J. Phys. Oceanogr.*, **23**, 1009–1039. Find this article online

Jones H., 1997: Restratification after deep convection. *J. Phys. Oceanogr.*, **27**, 2276–2287. Find this article online

LabSea Group,, 1998: The Labrador Sea Deep Convection Experiment. *Bull. Amer. Meteor. Soc.*, **79**, 2033–2058. Find this article online

Legg S., and J. Marshall, 1993: A heton model of the spreading phase of open-ocean deep convection. *J. Phys. Oceanogr.*, **23**, 1040–1056. Find this article online

Legg S., H. Jones, and M. Visbeck, 1996: A heton perspective of baroclinic eddy transfer in localized open ocean convection. *J. Phys. Oceanogr.*, **26**, 2251–2266. Find this article online

Lilly J., and P. Rhines, 2002: Coherent eddies in the Labrador Sea observed from a mooring. *J. Phys. Oceanogr.*, **32**, 585–598. Find this article online

Lilly J., M. Visbeck, R. Davis, J. Lazier, F. Schott, and D. Farmer, 1999: Observing deep convection in the Labrador Sea during winter 1994/95. *J. Phys. Oceanogr.*, **29**, 2065–2098. Find this article online

Madec G., M. Chartier, P. Delecluse, and M. Crepon, 1991: A three-dimensional numerical study of deep-water formation in the northwestern Mediterranean Sea. *J. Phys. Oceanogr.*, **21**, 1349–1371. Find this article online

Marshall J., and F. Schott, 1999: Open-ocean convection: Observations, theory, and models. *Rev. Geophys.*, **37**, 1–64. Find this article online

Maxworthy T., and S. Narimousa, 1994: Unsteady, turbulent convection into a homogeneous, rotating fluid, with oceanographic application. *J. Phys. Oceanogr.*, **24**, 865–887. Find this article online

MEDOC Group,, 1970: Observations of formation of deep water in the Mediterranean Sea, 1969. *Nature*, **227**, 1037–1040. Find this

Pedlosky J., 1979: *Geophysical Fluid Dynamics*. Springer, 625 pp.

Pickart R., 1992: Water mass components of the North Atlantic deep western boundary current. *Deep-Sea Res.*, **39**, 1553–1572. Find this article online

Schott F., M. Visbeck, and J. Fisher, 1993: Observations of vertical currents and convection in the central Greenland Sea during the winter of 1988/89. *J. Geophys. Res.*, **98**, 14401–14421. Find this article online

Send U., and R. Käse, 1998: Parameterization of processes in deep convection regimes. *Ocean Modeling and Parameterization,* E. Chassignet and J. Verron, Eds., NATO Science Series C, Vol. 516, Kluwer, 451 pp.

Send U., J. Font, and C. Mertens, 1996: Recent observation indicates convection's role in deep water circulation. *Eos, Trans. Amer. Geophys. Union*, **77**, 61–65. Find this article online

Talley L., and M. McCartney, 1982: Distribution and circulation of Labrador Sea water. *J. Phys. Oceanogr.*, **12**, 1189–1205. Find this article online

THETIS Group,, 1994: Open-ocean deep convection explored in the Mediterranean. *Eos, Trans. Amer. Geophys. Union*, **75**, 217–221. Find this article online

---

APPENDIX

5. Point Vortex Models

Point vortices are convenient for studying convective patch interactions with a side boundary. Equation (1) with $e = 0$ govern their evolution and the domain appears in Fig. 4 ⊙▪. The point vortex solution of (1) is written in integral form as

$$p_c(\mathbf{x}_o) = \iint G_c(\mathbf{x}_o; \mathbf{x})q_c(\mathbf{x})\, d\mathbf{x};$$

$$p_b(\mathbf{x}_o) = \iint G_b(\mathbf{x}_o; \mathbf{x})q_b(\mathbf{x})\, d\mathbf{x}, \qquad (A1)$$

where the Green's functions $G_{[b,c]}$ are

$$G_c(\mathbf{x}; \mathbf{x}_o) = -\frac{f_o}{2\pi}\left[K_o\left(\frac{|\mathbf{x} - \mathbf{x}_o|}{R}\right) - K_o\left(\frac{|\mathbf{x} - \mathbf{x}_o^i|}{R}\right)\right]$$

$$G_b(\mathbf{x}; \mathbf{x}_o) = \frac{f_o}{2\pi}[\ln(|\mathbf{x} - \mathbf{x}_o|) - \ln(|\mathbf{x} - \mathbf{x}_o^i|)]. \qquad (A2)$$

The point vortex location is $\mathbf{x}_o$, and its "image" is an equal distance inside the boundary at $\mathbf{x}_o^i$. The quantities $p_c = p_1 - p_2$, $q_c = q_1 - q_2$, $R^2 = (g_1 H_1 H_2)/[(H_1 + H_2)f_o^2]$, $p_b = H_1 p_1 + H_2 p_2$ and $q_b = H_1 p_1 + H_2 p_2$.

The point vortex approach proceeds by approximating (A1) discretely; for example,

$$p_c(\mathbf{x}_o) = \iint G_c(\mathbf{x}_o; \mathbf{x})q_c(\mathbf{x})\, d\mathbf{x}$$

$$= \sum_j q_{c,j}\delta A_j G_c(\mathbf{x}_o; \mathbf{x}_j), \qquad (A3)$$

where δA_j is the area element assigned to the potential vorticity anomaly $q_{c,j}$ and the summation is over all the point vortices. Send et al. (1996) report mean surface heat losses during the convection of a few hundred watts per square meter. Heat flux can be related to the strength of the potential vorticity anomalies, and their frequency of introduction into the fluid, following a procedure like that of Legg and Marshall (1993). The heat anomaly lost to the atmosphere from the ocean over a time interval δt and an area A_o due to a heat flux Q_f is $A_o Q_f \delta t$. The heat anomaly associated with a single baroclinic potential vorticity anomaly of the form in (A3) is

$$\rho_o C_p \Delta T \iint h_1 \, dA$$

$$= \rho_o C_p \Delta T \iint \frac{p_c}{g_1} \, d\mathbf{x}_o$$

$$= \frac{\rho_o C_p \Delta T f_o}{2\pi g_1} \iint q_{c,j} \delta A_j G_c(\mathbf{x}_o; \mathbf{x}_j) \, d\mathbf{x}_o$$

$$= -q_{c,j} \delta A_j R^2 \frac{\rho_o C_p \Delta T f_o}{g_1},$$

where C_p is the heat capacity of water and ΔT is the temperature difference between layers. If a convective anomaly is introduced into the interior every δt as a thickness perturbation with no circulation ([Gryanik et al. 2000](#)), the potential vorticity contributions to the two layers satisfy $q_{b,j} = 0$ and the required potential vorticity anomaly in the upper layer is

$$q_{1,j} \delta A_j = \frac{A_o Q_f \delta t g \alpha}{f_o R^2 \rho_o C_p (1 + H_1/H_2)},$$

where α is the thermal coefficient of expansion for seawater. The lower-layer amplitude, $q_{2,j}$, can be diagnosed from the barotropic constraint. Assuming heat fluxes of 250 W m^{-2} over a circular disk of radius 75 km (like observed), $\rho_o = 1000$ kg m^{-3}, $\alpha = -2 \times 10^{-4}/°$C, $g = 10$ m s^{-2}, $C_p = 4 \times 10^3$ J/(kg °C), $f_o = 10^{-4}$ s^{-1}, using the observationally motivated thicknesses $H_1 = H_2 = 1000$ m and employing $R_d = 10$ km yields typical anomaly strengths of $f_o q_{1,j} \delta A_j = 0.2$ m^2 s^{-2}.

Figures
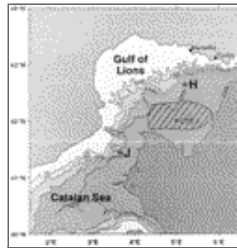
Click on thumbnail for full-sized image.

FIG. 1. Mediterranean convection setting. Convection typically occurs offshore of the Gulf of Lions in water depth of about 2000 m. The offshore slope is characterized by a depth change of 500 m over roughly 50 km. Nearer shore, the slope steepens to a 500-m change over roughly 10 km. The convection site is indicated by the hatched oval centered at 42°N, 5°E (after [Send et al. 1996](#))
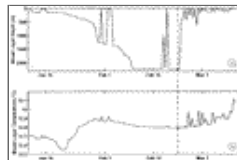
Click on thumbnail for full-sized image.

FIG. 2. Mixed layer evolution in the Mediterranean from [Send et al. (1996)](#): (a) mixed layer depth against time and (b) mixed layer temperature versus time, from a mixed layer simulation using realistic buoyancy fluxes. Mixed layer depth stagnates around 10 Feb at better than 2000 m, implying the convection has reached the bottom. Mixed layer temperature after that changes slowly. The period of deep convection is roughly one month

FIG. 3. Mixed layer remnants from the Labrador Sea. Note the thick layer between 200 and 2000 m, representing mixed layers from previous winters. Beneath this is a well-stratified column from 2000 to roughly 3500 m, indicating the convection in the Labrador Sea does not reach the bottom. Further, the density change under the mixed layer, in σ_θ, is 5–10 times that in the remnant mixed layers. Note also deep topographic slopes like those in the Mediterranean Sea. (From Marshall and Schott 1999)
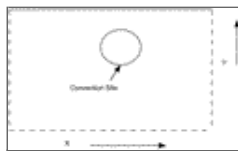
FIG. 4. A plan view of the model setup. The convection site is indicated by the closed circle and the domain boundary is given by the solid line to the north. The other boundaries, denoted by the dashed lines, can be either closed or open depending on the model type
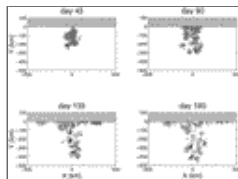
FIG. 5. Views of the evolution of a convective site as modeled using point vortices. The northern shading denotes the coast. Upper cyclones are denoted by circles and lower anticyclones by crosses. Note the rapid draining of the convection site effected by the image propagation
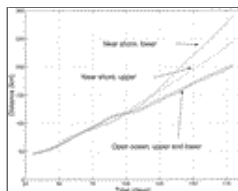
FIG. 6. Heton dispersion. Two experiments are compared; one with a nearby boundary, and one without. The two upper curves, labeled "Near shore," are from the experiment with a boundary, and the lowest curves are from the open-ocean experiment. The vortices' rms separation from the center of convection is plotted against time. The two upper curves are of the cyclonic and anticyclonic members, respectively. (The cyclonic member spread exceeds the anticyclonic spread because a heton impacted the boundary west of the convection site very early on. This is a statistical fluctuation.) Note that the near-shore dispersion exceeds that of the open ocean, due to the impact on the spread of the boundary images
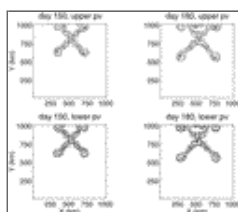
FIG. 7. Views of the upper- and lower-layer potential vorticities from a finite-difference QG model of the evolution of a convecting site. The upper layer appears in the upper panels and the lower layer in the lower panels. The behavior here mirrors that computed using point vortices; namely, the early evolution is dominated by heton formation followed by the hetons pairing with their images on the boundaries
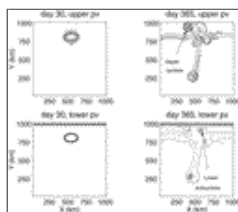
FIG. 8. Two views of the upper- and lower-layer potential vorticity from a two-layer run with a shelf break. The break appears as

the strong potential vorticity input on the northern boundary of the lower layer. The left column is from day 30, just after the convection has been completed. The right column is from day 365. Hetons form from the initial patch and have spread essentially east, west, north, and south. The first two are absent in the right-hand column, since only part of the domain has been shown. The northern heton, however, departs markedly from the behavior predicted by the flat-bottom case. As seen on day 365, the northern potential vorticity anomalies have largely stagnated, with at most some indication of westward spread of the upper-layer cyclone. The two heton members are indicated by the arrows
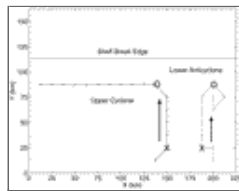
FIG. 9. Trajectories of the upper and lower heton members in an experiment with a shelf break. The cross marks denote roughly uniform time increments, vortex locations at day 130 are indicated by the "X," and at day 170 by the "O." Motion along the trajectories is indicated by the arrows and the trajectories end on day 365. The location of the leading edge of the shelf break is indicated
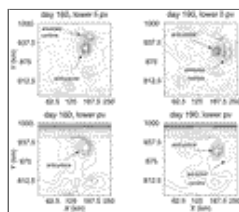
FIG. 10. Views of the lower layer interacting with a shelf break. The upper row displays anomalies of potential vorticity, and the lower row full potential vorticity, from days 160 and 190. These time bracket the period of vortex–shelfbreak interaction. On day 160, the anticyclone begins to extract high-potential-vorticity water from the break, which in turn develops a circulation that drives the vortex offshore. Note on day 190 the anticyclone has been pushed south and is separated from its previous cyclonic, surface-intensified companion. The arrows indicate the major features of the lower-layer potential vorticity fields
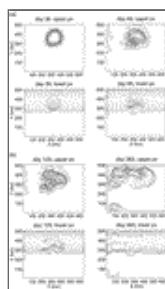
FIG. 11. Two-layer results with bottom topography. The bottom rises 500 m over the northern 250 km of the basin. The upper panels are of upper-layer potential vorticity and the lower panels of lower-layer potential vorticity. Days 30, 90, 120, and 365 are shown. Note that heton formation is disrupted by the topography and the convection spreads westward as directed by the topography
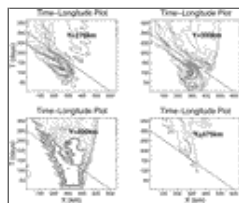
FIG. 12. Time–longitude plots at several latitudes of upper-layer potential vorticity anomalies are plotted. The solid line in each plot indicates a westward speed of 2 km day^{-1}. The latitudes to which the plots correspond are labeled in each panel and the same contour interval [1×10^{-6} (m s)$^{-1}$] is used in all plots
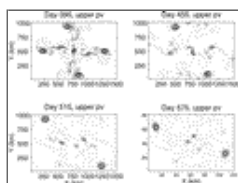
FIG. 13. Thickness and potential vorticity comparisons. Upper panels are upper-layer potential vorticity plan views from two different days. Lower panels are transects at latitude $Y = 400$ km (indicated by the solid line in the upper panels) of both potential vorticity and thickness (the potential vorticity has been multiplied by 10^7). The point of this comparison is that baroclinic wave propagation is a weak process and therefore thickness anomalies largely track potential vorticity anomalies. Note in the lower panel that sizeable interface deflections do not occur away from upper-layer potential vorticity anomalies
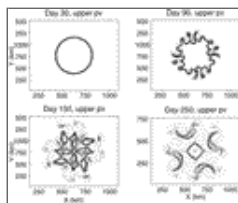
FIG. 14. Flat-bottom three-layer convective patch evolution. Upper-layer potential vorticity is shown in plan view; convectively formed potential vorticity is contoured using solid lines, and values close to the background value are dashed. Convection was modeled using an interfacial transfer between the upper two layers. The scale of the patch appears in the earliest plot. The developing instability appears at day 90, and is characterized by second-deformation-radius structures. The subsequent intermediate patch evolution is dominated by like-signed vortex pairing, and an associated upscale transfer in disturbance size

FIG. 15. Four later views of convective patch evolution in a three-layer model. Upper-layer potential vorticity is shown and the window into the domain has been expanded zonally relative to that in Fig. 14 . Essentially first mode hetons are evident at days 395 and 425. In fact, the northward and southward spreading hetons have contacted the domain boundaries and are coming under image influences. This appears in days 485 and 515, while the zonally migrating hetons have left the area. The subsequent evolution of the patch is now dominated by like-signed vortex merger, involving the remnant potential vorticity anomalies not dispersed from the convection site in first-mode hetons
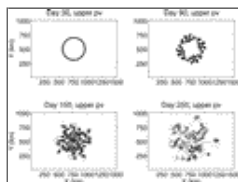
FIG. 16. Convective patch evolution in a three-layer model with a bottom slope. The slope is weaker than typical Labrador Sea slopes. Four different days are shown corresponding to early and intermediate patch evolution. Plan views of the upper-layer potential vorticity anomaly appear
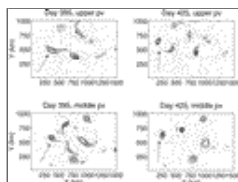
FIG. 17. Long-term patch evolution. Two later dates are shown from a three-layer run with a bottom slope. Upper- and midlayer potential vorticity anomalies appear in the upper and lower panels, respectively. The bulk of the anomalies are not found in heton formations for these dates, and the anomalies are on average smaller in scale than for a flat bottom. Rows indicate a hetonlike couple

FIG. 18. Comparisons of mass dispersal. Results from the flat-bottom and sloping-bottom runs are shown. The mass anomaly contained within a 200-km radius circle about the initial convection center has been computed and is plotted against time. The second year of the experiments are shown because that is the time at which first-mode hetons appear in the flat-bottom run. Note that the dispersal of the convective water is considerably less efficient with the sloping bottom than for the flat-bottom case, often by a factor of 4
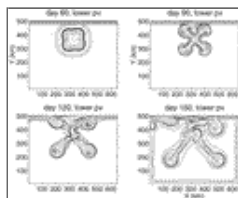
FIG. 19. Cyclonic vortex interaction with the shelf break. Here the bias of the thermocline anomaly was reversed, giving the cyclonic member the opportunity to interact with the shelf break. The bottom slope consisted of a rise of 250 m over the last 25 km. Note the cyclone is attracted to the slope and trapped there, principally by the on- and off-shelfbreak advections of background low-potential-vorticity waters
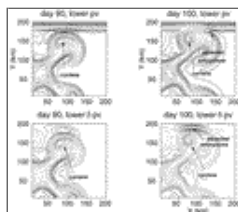
FIG. 20. Cyclone–shelfbreak interaction. The bottom shoals toward the side wall by 250 m over 25 km in this experiment. The panels show the interaction of the northeastern cyclone with the shelf break from Fig. 19 . The upper panel is of full lower-layer potential vorticity and the lower panel is of potential vorticity anomaly in the lower layer. The latter view suppresses the topographic input to potential vorticity. The days shown, 90 and 100, bracket the interesting period of interaction

Corresponding author address: Prof. William K. Dewar, Department of Oceanography, The Florida State University, Tallahassee, FL 32306-4320. E-mail: dewar@ocean.fsu.edu

top ▲